Journal of Aeronautical
-Science and Engineering-, Vol.5

February 28, 2016

Experimental Investigation and CFD Simulation of a Helicopter Tail Rotor Blade

Firdaus[a], Jaswar Koto[a,b,*], I.S. Ishak [a] and M.S. Ammoo[a]

[a)]*Department of Aeronautical, Automotive and Ocean Engineering, Faculty of Mechanical Engineering, Universiti Teknologi Malaysia*
[b)]*Ocean and Aerospace Engineering Research Institute, Indonesia*

*Corresponding author: jaswar@fkm.utm.my and jaswar.koto@gmail.com

Paper History

Received: 5-February-2016
Received in revised form: 18- February -2016
Accepted: 28- February -2016

ABSTRACT

This paper presents the experimental investigation and computational fluid dynamics (CFD) simulation of the generic model of the tail rotor blades from Bell 206B helicopter. Generally, the data about airfoil characteristics of the blade have been restricted by designers due to corporate secrets or copyright. Wind tunnel tests to investigate aerodynamic characteristics of tail blade were performed in the Universiti Teknologi Malaysia-Low Speed Tunnel (UTM-LST). CFD simulations of the tail blade in three dimensional (3D) were also carried out (ANSYS Fluent) on the same configuration. Both the experiments and the simulation were carried out at the same airspeed, set from 15 m/s to 40 m/s with increment of 5 m/s respectively and angle of attack (AOA) was set from 0, 5, 10, 12, and 15 degrees respectively in order to verify each other. Wind tunnel tests and computed results for the lift and drag were satisfactorily comparable. The empirical equation code was developed based on the curve fitting from the experimental results. The solutions of the empirical equation had good agreement.

KEY WORDS: *Experimental Investigation; Computational Fluid Dynamics (CFD); Wind tunnel test; Helicopter Tail Rotor Blades; Bell B206*; k–ω *Shear Stress Transport (SST) Model; FLUENT; Universiti Teknologi Malaysia-Low Speed Tunnel (UTM-LST).*

NOMENCLATURE

C_L	Lift coefficient
C_D	Drag coefficient
CFD	Computational Fluid Dynamic
AOA	Angle of Attack
SST	Shear Stress Transport

1.0 INTRODUCTION

The basic principle of wings, rotors and airscrews is that they accelerate a mass of air and that the resultant lift or thrust is the Newtonian reaction to that acceleration. Producing sufficient lift to permit a helicopter to fly is only a matter of having enough power to accelerate the air mass without excessive weight. A practical helicopter must, however, be able to control that lift precisely or it would be dangerous.

Any structure placed in a flow of air for the purpose of generating lift is called an aerofoil or airfoil. Aero planes and helicopters can fly when there is a wind blowing and can climb or lose height in the process. In helicopters the rotor blades have airspeed due to their rotation. Thus there can be situations where the airfoil moves through the air, or where the air moves past the airfoil. All that matters from the point of view of generating lift is the relative velocity and the direction from which it appears to be approaching the airfoil [1].

The rotor blade is the device that mainly used as propulsive for marine vehicles, airplanes and rotorcraft. As it is a crucial part, it has to be designed to attain power requirement at the indicated velocity with optimum efficiency. Now days, with

increasing demands for of more power and higher speed, the rotor blade is becoming progressively larger in size and its geometric shape become more complicated. Due this complicated geometry, the rotor blade need be optimally designed for improved propulsion efficiency.

Helicopters with a single main rotor must have some means of balancing the torque reaction due to driving the rotor. Whilst the anti-torque rotor could be mounted anywhere for hovering, in forward flight the most stable location is aft, supported on some kind of structure called a boom. In addition to the anti-torque function helicopters need some means of yaw control and the tail rotor also serves that purpose. In order to balance the weight of machinery at the tail, the helicopter cabin usually extends some way forward of the mast. This large forward side area is unstable in yaw and generally some fin area is needed to give directional stability in forward flight. A further consideration is that the main rotor on its own is unstable in pitch in forward flight and a tail plane is usually required.

The first difficulties helicopter engineers faced when tried to build a helicopter that can hover was the problematic of torque reaction [2]. The third law of motion of Newton's involves, for each act there is an opposed and equal action. Normally, a single main rotor of helicopter has a rotor system attached on a rotor mast. The produced power by the engine so that the helicopter can rotate the mast, and so the rotor component system that connected to it. When the torque applies to rotation of the mast, there is torque reaction which an opposite and equal amount happen, which attempts to yaw the helicopter in the opposed way as shown in Figure 1.

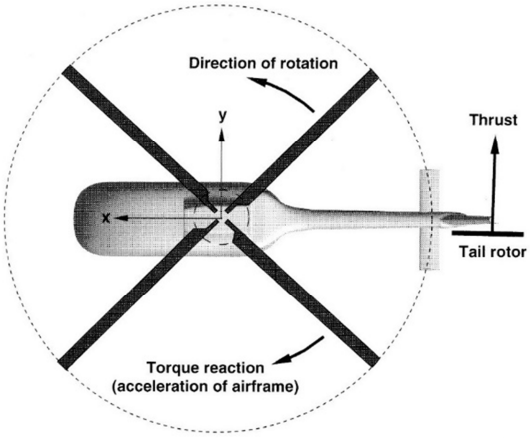

Figure 1 Torque reaction is in the opposite direction [5]

Seems Igor Sikorsky is the first individual to resolve on with a single rotor attached at the tail boom, stern of the helicopter as a way anti- torque. Despite, he already experimented with many variation of arrangements before choosing a single tail attached rotor. Now day, this arrangement is the most popular, seems that the many of helicopters manufacturer using this technique of countering torque, given that there are several main complications with this technique which are not encountered with counter-rotating of rotor systems [3].

One main problematic with tail rotors is consume massive sum of the engine power. The tail rotors devour up to 30% of the engine power [4] as a rule of thumb.

The difficult with the tail rotors is that properly difficult to switch perfectly. Crosswinds and turbulence make it tremendously difficult to hold a steadily heading of the helicopter that equipped with the tail rotor. Furthermore, it is very high in workload, and to achieve better results are tough. In the end, numerous larger helicopters presence designed with a yaw stabilization system, which is fundamentally an autopilot for the tail rotor.

For this research, the performance characteristics of helicopter tail rotor blade will be determined via experimental in the Universiti Teknologi Malaysia-Low Speed Tunnel (UTM-LST), numerical simulation and the empirical method. Finally, the results were compared to find the correlation between the experimental, empirical and simulation works.

2.0 BACKGROUND WORKS

2.1 Generic Tail Rotor Blades

Real-world rotor blade engineers usually search for compromises between good hovering behavior and forward flight efficiency, in addition to light loads, low noises, reduced vibrations, etc. Rotor blades usually have high aspect ratios, to reduce drag forces due to blade tip vortices, where aspect ratios are the lengths of blade spans to those of chords. Airflow is fastest at the blade tips and easy to generate vortices acting as downward drag forces. These downward drag forces are degraded as the aspect ratios increased.

The blades used in this study was from generic model of the tail rotor blades from Bell 206B helicopter, with an actual scale as shown in Figure 2. The dimension of the blade was 720 mm overall length and has 134 mm length of the chord. The coordinates of the blade have been measured accurately using the available instrument in the UTM Aeronautic laboratory and the coordinates were plotted in 3D models using *Autodesk AutoCAD* software as shown in Figure 3.

Figure 2 The generic model of tail rotor blade for Bell B206 [6]

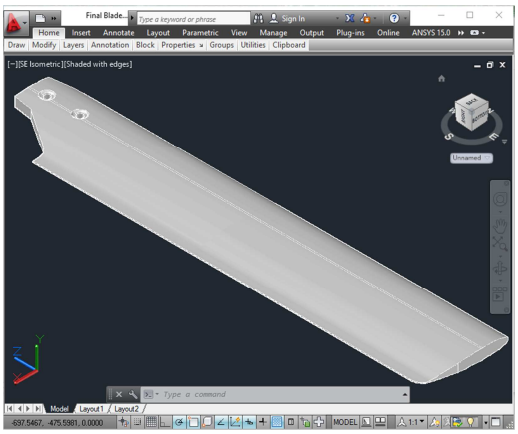

Figure 3 The 3D CAD model of tail rotor blade

The airfoil profile of the blade is near similar to NACA 0012 series, with maximum thickness 12% at 33% chord as shown in Figure 4.

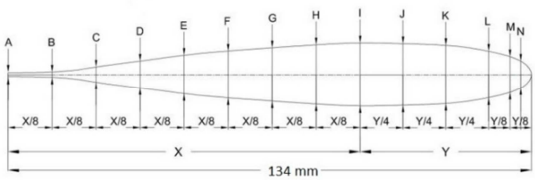

Figure 4 Airfoil profile of tail rotor blade

3.0 THEORETICAL BACKGROUND

3.1 Blade Element Theory

Consider a component of a blade of chord, (c) with width, (δr) at a blade radius, (r) from the center of rotation. This component of the blade has a velocity in the plane of revolution of Ωr. If the propeller blade is advancing at a velocity of V_C, then the local induced velocity is vi. The total speed of the flow relative to the propeller blade is V_R, as indicate in Figure 5.

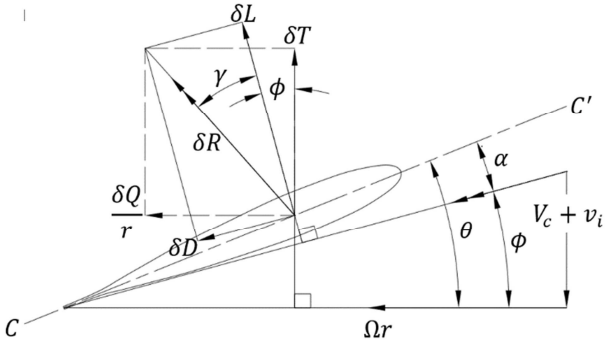

Figure 5 Velocities and forces on a blade element (E.L. Houghton, 2013)

If the axis line of CC' denotes the zero-lift line of the propeller blade segment, therefore, the geometric helix or pitch angle of the component that represented by θ, and the absolute angel of incidence of the segment represented by α. The lift and drag forces that consequently experienced by element, correspondingly vertical and matching to the relative velocity (V_R), fitting to the absolute incidence of α. This lift force and drag force may be determined into components of thrust and "toque-force" that indicated in Figure 5, where δL is the lift force and δD is the drag force on the component. And δR is the resultant aerodynamics force, creating the angle γ with the lift vector. Lastly, δR as fixed into components of thrust, (δT) and torque force, $(\delta Q/r)$, where δQ is the torque necessary to turn the component around the propeller blade center of rotation [7].

$$\tan\gamma = \frac{\delta D}{\delta L} = \frac{C_D}{C_L} \tag{1}$$

$$V_R = (V_C + v_i)\ \csc\phi = \Omega r\ \sec\phi \tag{2}$$

$$\delta T = \delta R\cos(\phi+\gamma) \tag{3}$$

$$\frac{\delta Q}{r} = \delta R\sin(\phi+\gamma) \tag{4}$$

$$\tan\phi = \frac{V_c + v_i}{\Omega r} \tag{5}$$

The element of η_1 is the efficiency by the ratio of useful power out to power in:

$$\eta_1 = \frac{V}{\Omega}\frac{\delta T}{\delta Q} = \frac{V\cos(\phi+\gamma)}{\Omega r\sin(\phi+\gamma)} \tag{6}$$

Let assume that the slope of lift, (a) of the segment is constant so that, if the segment incidence (α) is determined from the no-lift line, can be show:

$$C_L = a\alpha = a(\theta-\phi) \tag{7}$$

Empirical data recommends a lift slope (a) of around 5.7 [8].

So, the solidity of the annulus σ be distinct as the fraction of the total area of propeller blades in the annulus to the entire area of annulus. Then

$$\sigma = \frac{Bc}{2\pi r}\frac{\delta r}{\delta r} = \frac{Bc}{2\pi r} \tag{8}$$

where the total number of blades indicated by B
Then

$$\delta L = Bc\delta r\frac{1}{2}\rho V_R^2 C_L \tag{9}$$

$$\delta D = Bc\delta r\frac{1}{2}\rho V_R^2 C_D \tag{10}$$

From Figure 5

$$\delta T = \delta L\cos\phi - \delta D\sin\phi$$
$$= Be\delta r\frac{1}{2}\rho V_R^2(C_L\cos\phi - C_D\sin\phi) \tag{11}$$

Therefore,

$$\frac{dT}{dr} = Bc\frac{1}{2}\rho V_R^2(C_L\cos\phi - C_D\sin\phi)$$
$$= 2\pi r\sigma\frac{1}{2}\rho V_R^2(C_L\cos\phi - C_D\sin\phi) \tag{12}$$

Bering in mind Equation (1), Equation (13) may written as

$$\frac{dT}{dr} = \pi r\sigma\rho V_R^2 C_L(\cos\phi - \tan\gamma\sin\phi)$$
$$= \pi r\sigma\rho V_R^2 C_L\sec\gamma\ (\cos\phi\cos\gamma - \sin\phi\sin\gamma) \tag{13}$$

At present, for moderate incidence of the propeller blade section, $tan\,\gamma$ is small number around 0.02. That is, L/D ≈ 50,

and therefore $sec\,\gamma \approx 1$. In this case the previous equation may be written as

$$\frac{dT}{dr} = \pi r \sigma \rho V_R^2 C_L \cos(\phi + \gamma) \tag{14}$$

Let

$$t = C_L \cos(\phi + \gamma) \tag{15}$$

Then, thrust for the rotor blade (used in this study for thrust calculation)

$$\frac{dT}{dr} = \pi r \sigma t \rho V_R^2 = Bc\frac{1}{2}\rho V_R^2 t \tag{16a}$$

For per blade

$$\frac{dT}{dr} = c\frac{1}{2}\rho V_R^2 t \tag{16b}$$

Defining a thrust coefficient by

$$C_T = \frac{T}{\rho n^2 D^4} \tag{17}$$

Where n is the rotor blade rotational speed in (rev/s) and D in diameter of rotor.

Similarly,

$$\frac{\delta Q}{r} = \delta L \sin\phi + \delta D \cos\phi \tag{18}$$

Whence, using Equation (9) and Equation (10),

$$\frac{dQ}{dr} = 2\pi r^2 \sigma \frac{1}{2}\rho V_R^2 (C_L \sin\phi + C_D \cos\phi) \tag{19}$$

Let

$$q = C_L \sin(\phi + \gamma) \tag{20}$$

Which leads to, total torque for the rotor blade (used in this study torque calculation)

$$\frac{dQ}{dr} = \pi r^2 \sigma q \rho V_R^2 = Bcr\frac{1}{2}\rho V_R^2 q \tag{21a}$$

For per blade

$$\frac{dQ}{dr} = cr\frac{1}{2}\rho V_R^2 q \tag{21b}$$

Defining a torque coefficient C_Q by

$$C_Q = \frac{Q}{\rho n^2 D^5} \tag{22}$$

3.2 Basic Transport Equations

The Navier-Stokes equations, describing momentum conservation, are taken in their transient, 2D form, taking as variables the space x and z and velocity u and w velocity components. Their formulation is:

$$\frac{\partial(\rho u)}{\partial t} + \frac{\partial}{\partial x}(\rho u^2) + \frac{\partial}{\partial z}(\rho u w) = \frac{\partial}{\partial x}\left[\Gamma\left(2\frac{\partial u}{\partial x} - \frac{2}{3}div\vec{V}\right)\right] + \frac{\partial}{\partial z}\left[\Gamma\left(\frac{\partial u}{\partial z} + \frac{\partial w}{\partial x}\right)\right] - \frac{\partial p}{\partial x} \tag{23}$$

$$\frac{\partial(\rho w)}{\partial t} + \frac{\partial}{\partial x}(\rho u w) + \frac{\partial}{\partial z}(\rho w^2) = \frac{\partial}{\partial z}\left[\Gamma\left(2\frac{\partial w}{\partial z} - \frac{2}{3}div\vec{V}\right)\right] + \frac{\partial}{\partial x}\left[\Gamma\left(\frac{\partial u}{\partial z} + \frac{\partial w}{\partial x}\right)\right] - \frac{\partial p}{\partial z} \tag{24}$$

where p is pressure and Γ is the total viscosity, which includes the contributions of the dynamic and turbulent components Γ, i.e. $\Gamma = \mu + \mu_t$. The three unknowns u, w, and p in these equations need the mass conservation equation to close the problem:

$$\frac{\partial \rho}{\partial t} + \frac{\partial}{\partial x}(\rho u) + \frac{\partial}{\partial z}(\rho w) = 0 \tag{25}$$

The turbulent viscosity is solved with the turbulence model. The k-ε and the SST models, described next sub-section.

3.3 The k-ε Turbulence Model

The standard formulation of the k-ε model is described in [2]. The turbulent viscosity is given by:

$$\mu_t = C_\mu \frac{\rho k^2}{\varepsilon} \tag{26}$$

The turbulence kinetic energy, k, and its dissipation rate, ε, are computed with the following transport equations:

$$\frac{\partial(\rho k)}{\partial t} + \frac{\partial}{\partial x}(\rho u k) + \frac{\partial}{\partial z}(\rho w k) = \frac{\partial}{\partial x}\left[\left(\mu + \frac{\mu_t}{\sigma_k}\right)\frac{\partial k}{\partial x}\right] + \frac{\partial}{\partial z}\left[\left(\mu + \frac{\mu_t}{\sigma_k}\right)\frac{\partial k}{\partial z}\right] + P_k - p\varepsilon \tag{27}$$

$$\frac{\partial(\rho \varepsilon)}{\partial t} + \frac{\partial}{\partial x}(\rho u \varepsilon) + \frac{\partial}{\partial z}(\rho w \varepsilon) = \frac{\partial}{\partial x}\left[\left(\mu + \frac{\mu_t}{\sigma_\varepsilon}\right)\frac{\partial \varepsilon}{\partial x}\right] + \frac{\partial}{\partial z}\left[\left(\mu + \frac{\mu_t}{\sigma_\varepsilon}\right)\frac{\partial \varepsilon}{\partial z}\right] + \frac{\varepsilon}{k}(C_l P_k - C_2 \rho \varepsilon) \tag{28}$$

where P_k is the production rate of k as the results of the velocity gradients:

$$P_k = \mu_t\left[2\left(\frac{\partial u}{\partial x}\right)^2 + 2\left(\frac{\partial w}{\partial z}\right)^2 + 2\left(\frac{\partial u}{\partial z} + \frac{\partial w}{\partial x}\right)^2\right] \tag{29}$$

The remaining model constants are:

$C_\mu = 0.09 \quad \sigma_k = 1.0 \quad \sigma_\varepsilon = 1.3 \quad C_1 = 1.44 \quad C_2 = 1.92$

3.4 The k-ω SST Turbulence Model

The *SST* model [3] represents a combination of the $k-\varepsilon$ and the $k-\omega$ models, taking benefit of the advantages of each of these models. The $k-\omega$ model is more accurate near the wall but presents a high sensitivity to the ω values in the free stream region, where the $k-\varepsilon$ model shows a better behavior. The *SST* model blends the $k-\varepsilon$ and the $k-\omega$ by using a weighting factor based on the nearest wall distance. The governing equations are:

$$\frac{\partial(\rho k)}{\partial t} + \frac{\partial}{\partial x}(\rho u k) + \frac{\partial}{\partial z}(\rho w k) = \overline{P_k} - \beta^* \rho \omega k + \frac{\partial}{\partial x}\left((\mu + \sigma_k \mu_t)\frac{\partial k}{\partial x} + \frac{\partial}{\partial z}(\mu + \sigma_k \mu_t)\frac{\partial k}{\partial z}\right) \tag{30}$$

$$\frac{\partial(\rho \omega)}{\partial t} + \frac{\partial}{\partial x}(\rho u \omega) + \frac{\partial}{\partial z}(\rho w \omega) = \frac{\partial}{\partial x}\left((\mu + \sigma_\omega \mu_t)\frac{\partial \omega}{\partial x}\right) + \frac{\partial}{\partial z}\left((\mu + \sigma_\omega \mu_t)\frac{\partial \omega}{\partial z}\right) + \frac{\alpha \bar{P}_k}{v_t} - \beta \rho \omega^2 + 2(1 - F_1)\rho \sigma_{\omega 2}\frac{1}{\omega}\left(\frac{\partial k}{\partial x}\frac{\partial \omega}{\partial x} + \frac{\partial k}{\partial z}\frac{\partial \omega}{\partial z}\right)$$

(31)

where ω is the frequency of dissipation of turbulent kinetic energy [s^{-1}]. The production of turbulent kinetic energy is limited to prevent the build-up of turbulence in stagnant regions:

$$\bar{P}_k = \min(P_k, 10\beta^*\rho k\omega) \quad (32)$$

The weighting function *F1* is given by:

$$F_1 = tanh\left\{\left\{min\left[max\left(\frac{\sqrt{k}}{\beta^*\omega y}; \frac{500v}{y^2\omega}\right); \frac{4\rho\sigma_{\omega 2}k}{CD_{k\omega}y^2}\right]\right\}^4\right\} \quad (33)$$

$$CD_{k\omega} = max\left(2\rho\sigma_{\omega 2}\frac{1}{\omega}\frac{\partial k}{\partial x_j}\frac{\partial \omega}{\partial x_j}, 10^{-10}\right) \quad (34)$$

where *y* represents the distance to the neighbour wall and ν is the laminar dynamic viscosity. *F1* is zero away from the wall (*k*-ε model) and changes to unit inside the boundary layer (*k*-ω model). The turbulent viscosity is given by:

$$v_t = \frac{a_1 k}{max(a_1\omega; SF_2)} \quad (35)$$

where *S* represents the invariant measure of the strain rate:

$$S = \sqrt{S_{ij}S_{ij}} \quad ; \quad S_{ij} = \frac{1}{2}\left(\frac{\partial u_i}{\partial x_j} + \frac{\partial u_j}{\partial x_i}\right) \quad (36)$$

$$F_2 = tanh\left\{\left[max\left(\frac{2\sqrt{k}}{\beta^*\omega y}; \frac{500v}{y^2\omega}\right)\right]^2\right\} \quad (37)$$

The constants are computed as a blend of the *k*-ε and the *k*-ε models, through the following generic equation:

$$\alpha = F_1\alpha_1 + (1 - F_1)\alpha_2 \quad (38)$$

The constants are $\alpha 1 = 5/9$; $\beta 1 = 3/40$; $\sigma k1 = 0.85$; $\sigma\omega 1 = 0.5$; $\alpha 2 = 0.44$; $\beta 2 = 0.0828$; $\sigma k2 = 1$; $\sigma\omega 2 = 0.856$; $\beta* = 0.09$.

3.5 The Empirical Method

3.5.1 Performance Computation (Thrust and Torque)

The thrust and torque coefficients can be expressed as functions of the blade number, blade area ratio, pitch ratio, and advance coefficient:

$$C_T = \sum_{n=1}^{39} K_{T_n} J^{aj_n}\left(\frac{P}{D}\right)^{r_n}\left(\frac{A_D}{A_O}\right)^{a_n} Z^{z_n} \quad (39)$$

$$C_Q = \sum_{n=1}^{47} K_{Q_n} J^{aj_n}\left(\frac{P}{D}\right)^{r_n}\left(\frac{A_D}{A_O}\right)^{a_n} Z^{z_n} \quad (40)$$

where:

K_{T_n} is the regression coefficients of the thrust
K_{Q_n} is the regression coefficients of the torque
aj_n is the exponents of advance coefficient, J
r_n is the exponents of pitch ratio, (P/D)
a_n is the exponents of blade area ratio, (A_D/A_O)
z_n is the exponents of number of blade, Z

The values of these coefficients are all shown in Table 1. The performance characteristics of thrust T, and torque Q can, thus, be calculated using these values and from the equations (17) and (22) can be written by:

$$T = C_T\rho n^2 D^4 \quad (41)$$
$$Q = C_Q\rho n^2 D^5 \quad (42)$$

where
ρ is the density of fluid (kg/m^3)
n is the number of rotational of blade (rev/s)
D is the diameter of the blade (m)

The value coefficient in Table 1 was based on the correlation, and regression analysis for curve fitting of B-series propellers were developed in the Netherlands Ship Model Basin by Benini E (2003).

To get the value, the original coefficient was used the technique of correlation to test the statistical significance of the association with the new experimental data (tail blade). The experimental data of tail blade was plotted in Microsoft Excel and the slope of a line obtained using linear least squares fitting to obtain the new coefficient of the regression. The new coefficient was used as foundation of the computer programming in the next subsection to calculate the performance of the tail blade.

4.0 SIMULATION AND EXPERIMENTAL WORKS

The methodology adopted to conduct the study consists of several steps. The first and foremost was to obtain the coordinate measurements of blade section geometry. The coordinates of the blade have been measured accurately using the available instrument in the UTM Aeronautic laboratory and were plotted using *Autodesk AutoCAD* software. The next step was to construct the aluminum bracket was used to hold and appointed the airfoil blade in the wind tunnel's test section. The position of bracket in wind tunnel's section is shown is Figure 6. To measure the aerodynamic characteristics, lift, drag and pitching-moment, the tail rotor blade was supported by a bracket has been attach to force balance sensor. Figure 6 shows the schematic diagram of the tail rotor blade configuration in this experiment that mounted on force balance sensor via bracket support.

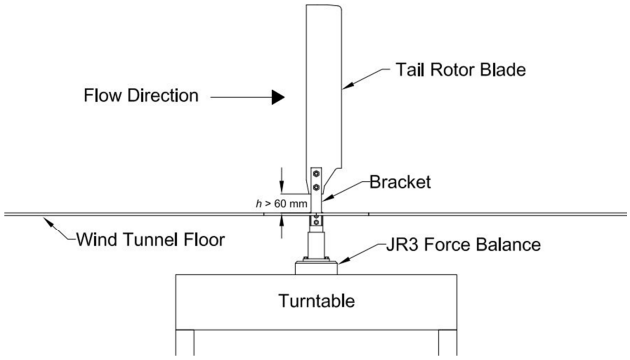

Figure 6 Schematic diagram of blade arrangement

The plotted blade geometry was also used in the CFD simulation. ANSYS meshing software was used to produce the necessary mesh. The setup was then simulated using ANSYS Fluent CFD software and the CFD simulation was carried out with various physical models, numerical algorithms, a discretization method and boundary conditions. In the final step,

the study was wrapped up by comparing the computed and measured results in a further investigation of the blade aerodynamics characteristics.

4.1 Wind Tunnel Testing

Several stages of wing tunnel experimental were performed on the Bell 206B helicopter tail rotor blades in Universiti Teknologi Malaysia –low speed wind tunnel (UTM-LST).

The UTM-LST is a pressurized, closed-circuit, continuous-flow wind tunnel with an operating pressure from approximately 0.10 to 4 atmospheres. The test section size is 2.0 m wide x 1.5 m height x 5.5 m length. The wind tunnel has an excellent flow quality (flow uniformity < 0.15%, temperature uniformity < 0.2%, flow angularity uniformity < 0.15%, turbulence < 0.06%) that was mentioned in the AIAA paper [9]. And it is capable of delivering maximum airspeed of 80 m/s (160 knots or 288 km/hr) inside the test section [10].

Table 1 Regression coefficient and exponents of C_T and C_Q, which use in this empirical equation to programming this application

n	K_{Tn}	aj_n	r_n	a_n	z_n	n	K_{Qn}	aj_n	r_n	a_n	z_n
1	0.010213754	0	0	0	0	1	0.003720841	0	0	0	0
2	-0.23728264	1	0	0	0	2	0.008695018	2	0	0	0
3	0.19296716	0	1	0	0	3	-0.03162197	1	1	0	0
4	0.18341224	0	2	0	0	4	0.003381583	0	2	0	0
5	-0.17119396	2	0	1	0	5	-0.04009618	0	1	1	0
6	-0.55853652	1	1	1	0	6	-0.10593523	1	1	1	0
7	0.42981112	0	2	1	0	7	-0.08454503	2	1	1	0
8	0.014902689	0	0	0	1	8	0.180056899	0	2	1	0
9	-0.05483939	2	0	0	1	9	-0.00354145	1	0	0	0
10	0.014844544	0	1	0	1	10	0.004905283	0	1	0	1
11	0.062782218	1	1	0	1	11	0.020000285	1	1	0	0
12	-0.02219134	0	0	1	1	12	0.002917536	2	1	0	0
13	0.01933488	1	0	1	1	13	-0.00444968	2	0	1	1
14	-0.23566946	0	3	0	0	14	0.002696525	1	1	1	1
15	0.0112532	0	6	0	0	15	-0.01657098	0	2	1	1
16	-0.00233942	2	6	0	0	16	0.055914236	3	0	1	0
17	0.161486566	3	0	1	0	17	0.016219358	0	3	1	0
18	-0.04861139	0	0	2	0	18	0.003186904	1	3	1	0
19	0.081900935	2	0	2	0	19	0.015926202	0	0	2	0
20	-0.04834888	3	0	2	0	20	0.042380133	1	0	2	0
21	0.005412498	1	6	2	0	21	0.017634065	3	0	2	0
22	-0.00335286	2	6	2	0	22	-0.04516993	0	1	2	0
23	-0.00435342	0	3	0	1	23	-0.02700141	3	1	2	0
24	0.027082579	1	3	0	1	24	0.041687173	2	2	2	0
25	-0.00164492	3	3	0	1	25	-0.03974834	0	3	2	0
26	-0.05110079	0	3	1	1	26	-0.00349814	0	6	2	0
27	0.015737124	1		2	1	27	-0.00871501	3	0	0	1
28	-0.00347494	0	2	2	1	28	0.000904525	3	3	0	1
29	-0.00051333	0	0	0	2	29	-0.00025603	0	6	0	1
30	-0.00421419	1	0	0	2	30	0.002934937	3	0	1	1

31	0.00620604	2	0	0	2	31	-0.00149625	0	6	1	1
32	-0.00133882	3	0	0	2	32	-0.00403893	1	0	2	1
33	-0.00390883	1	2	0	2	33	0.01334982	0	2	2	1
34	-0.00037676	1	6	0	2	34	-0.00243833	2	3	2	1
35	0.0001335	2	6	0	2	35	0.002560827	0	6	2	1
36	0.000791707	0	0	1	2	36	-0.00140572	1	1	0	2
37	0.012362728	0	3	1	2	37	0.000158601	3	2	0	2
38	1.66E-04	3	6	1	2	38	-4.19E-05	3	6	0	2
39	-0.00429623	0	3	2	2	39	0.000380175	1	0	1	2
						40	-7.8103E-05	2	0	1	2
						41	-0.0001457	0	2	1	2
						42	-2.8392E-05	0	6	1	2
						43	-0.00036807	0	0	2	2
						44	-0.00084956	0	3	2	2
						45	1.74E-04	3	3	2	2
						46	0.000105433	0	6	2	2
						47	-1.25E-05	1	6	2	2

There are four important components in the wind tunnel called test section, fan-motor, fan diffuser and settling chamber. The layout of wind tunnel aerodynamics circuit and indicates the important components within the wind tunnel circuit are illustrated in Figure 7.

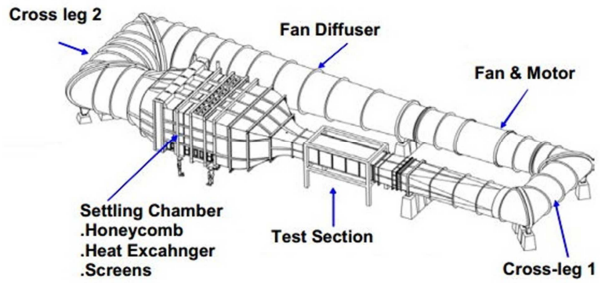

Figure 7 Wind tunnel components arrangement

The wind tunnel speed was set from 15 m/s to 40 m/s and angle of attack of 0, 5, 10, 12, 15, 18, 20, and 25 degrees at each speed. Aerodynamic forces such as lift and drag were obtained from the tests will be plotted coefficient against different angles of attack. Since the blockage ratio is merely small, blockage corrections are assumed to be negligible.

The dynamic pressure for each speed can be calculated by equation below [11]:

$$p_d = \frac{1}{2}\rho V^2 \tag{43}$$

where:

p_d is the dynamic pressure (Pa)
ρ is the density of fluid (kg/m^3)
V is the velocity of air (m/s)

And another important parameter is Reynolds number which can be calculated using equation below:

$$Re = \frac{\rho VL}{\mu} = \frac{VL}{\nu} \tag{44}$$

where *Re* is the non-dimensional Reynolds Number, ρ is the density of air (kg/m3), μ is the dynamic viscosity (Ns/m2) of the fluid, ν is the kinematic viscosity (m2/s), V is the air speed (m/s) and L is characteristic length (travelled length of the fluid) (m) which in this case based on the length of the airfoil chord.

Table 2 shows the set up air speed data from the wind tunnel, corresponds to a Reynolds number based on airfoil chord.

Table 2 Wind tunnel air speed data

Speed (m/s)	RPM	Dynamic Pressure (Pa)
15	152.5	131.6
20	200.5	234.0
25	249.0	365.6
30	297.0	526.5
35	345.0	716.6
40	393.0	936.0

4.2 Computational Fluid Dynamic Simulation

4.2.1 Domain and Boundary Conditions

Before execute the simulation work, a fluid domain was created which define boundary conditions in the simulation models. Then, followed by the mesh generation for the models that will be simulated with selected turbulence model.

In AutoCAD, 3D block domain has been generated which the dimension of the block similar as the dimension of the test section of Universiti Teknologi Malaysia- Low Speed Tunnel (UTM-LST) (2.0 m wide x 1.5 m height x 5.5 m length) with the 3D CAD model of tail rotor blade was placed in it. Then, all the 3D models were exported to Geometry Modeler in ANSYS package and the 3D model of tail blade was subtracted from the block to create a "mould", as shown in Figure 8.

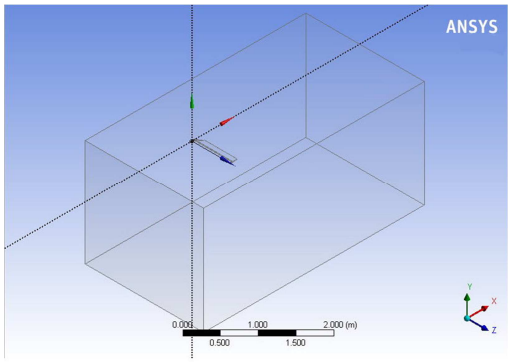

Figure 8 3D block geometry in ANSYS Geometry Modeler

In Figure 9, the solid block indicates the fluid domain and the tail blade model was a hollow space embedded in it. In the ANSYS Fluent software, the solid area was defined as the fluid (air) while the hollow space is the solid model (tail blade).

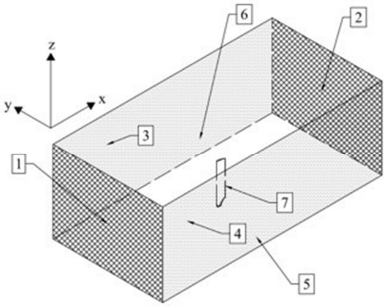

Faces	Type
1-Front	Velocity Inlet
2-Back	Pressure Outlet
3-Side 1	Symmetry
4-Side 2	Symmetry
5-Bottom	Wall
6-Top	Symmetry
7-Innerbody	Wall

Figure 9 Boundary conditions of 3D block geometry

The computational fluid domain has 630,727 nodes and 2,536,280 elements. Figure 10 show the meshing at the surface of the rotor blade that generated by ANSYS Mesh. In order to show the detailed structure of the meshing around the rotor blade region, the magnified images of the mesh are shown in the Figures 11. The detailed distribution of the tetrahedrons and wedges are clearly seen in these figures:

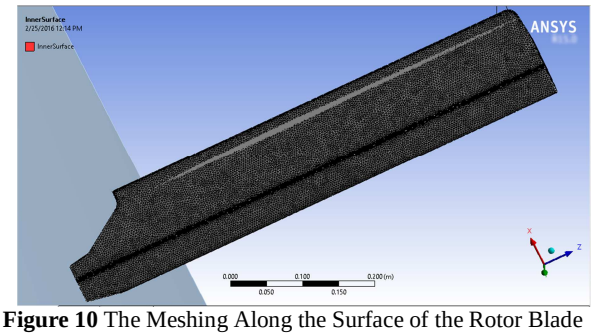

Figure 10 The Meshing Along the Surface of the Rotor Blade

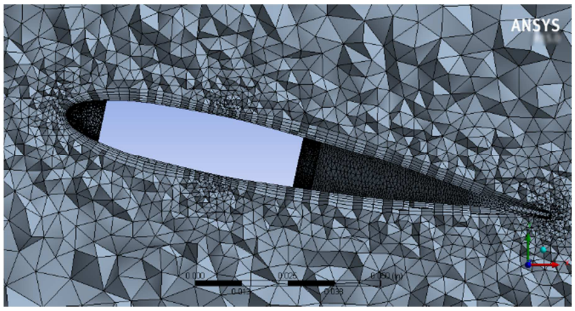

Figure 11 Close-up view of the meshing around the blade model

The k-ω Shear Stress Transport (SST) of transition model are used in these simulations, as well as the hybrid and the Quick advection schemes.

To confirm the current simulation procedure, the working conditions are imitated to identical the working situations of the experimental works conducted previously in the Universiti Teknologi Malaysia- Low Speed Tunnel [6]. The velocity inlet (Figure 12) for the simulation was set from 15 m/s to 40 m/s and angle of attack of 0, 5, 10, 12, 15, 18, 20, and 25 degrees. The temperature of free stream is 298.65 K, which is the similar as the surrounding temperature of air. The density of the air is $\rho = 1.17kg/m3$ and the viscosity is $\mu = 1.859 \times 10^{-5} kg/s \cdot m$ at the given temperature.

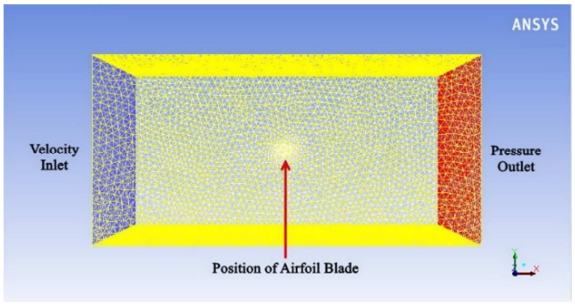

Figure 12 Domain mesh of ANSYS Fluent simulation

In this simulation work, it is presumed that velocity inlet is similar turbulent as pressure outlet. So, for velocity inlet of boundary condition turbulent concentration is considered 5% and for the pressure outlet of boundary is also considered 5% as recommended by ANSYS Fluent (2013), which state the inlet boundary condition turbulence intensities is ranging from 1% to 5% [12]. In addition, turbulent viscosity was set to 10 for a better approximation of the problem as recommended by ANSYS Fluent (2013). The blockage ratio is defined as the ratio of the frontal area of the blockage, to the cross-section area of the wind tunnel. Since the computational domain was design same as the dimension of the test section of the wind tunnel, the blockage ratio was known that less than 0.1% and it is shown that the effects of blockage on pressure distribution and the drag coefficient are very small.

5.0 RESULTS

5.1 Wind Tunnel Testing Results

Graph in Figure 13 shows the lift coefficient characteristics with different wind speed. At an angle of attack 12-13 degree shows the peak of lift coefficient where maximum lift happens before it drops after this point. And this condition is a critical or stalling angle of attack where the tail rotor blade starts to be less efficient to generate lift after beyond this angle of attack. Lift get higher when the velocity of air was increase can be proved based on equation, $F_L = \frac{1}{2} C_L \rho V^2 s$, where F_L is the lift , ρ is the density of fluid, V is the velocity of air and S is the cross sectional area of the airfoil. Concluded that the lift increase corresponding with increasing of airspeed.

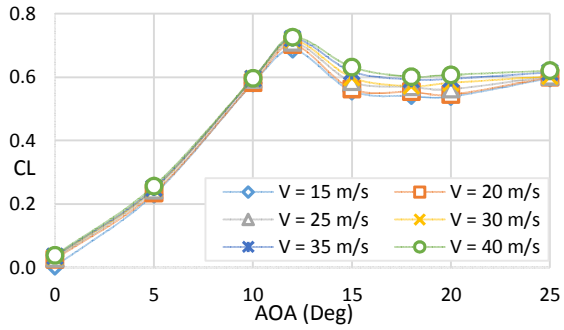

Figure 13 Lift coefficient versus angle of attack

The stall phenomena happened as the flow stared to separate where the air under heavier pressure beneath the blade finds it is easier to creep forwards over the upper surface from the trailing edge as the angle against the relative airflow increases, because the upper air has started to slow down and now has an unfavorable pressure gradient, past the suction peak. It has longer to travel and more surface friction to cope with, so it doesn't have the energy to keep flowing and create the same pressure differential, and the amount of lift is reduced (the pressure at the trailing edge is atmospheric anyway). As the boundary layer has less momentum, it works harder keeping to surface.

Boundary layer separation is therefore produced from the adverse pressure gradient, when air start flowing in the reverse direction of the free stream, forcing itself under the normal airflow which has started to slow down. This flow we can see through the smoke and oil dot test like in Figure 14. This test will show the patterns of airflow on the blade, before and after stalling angle happen.

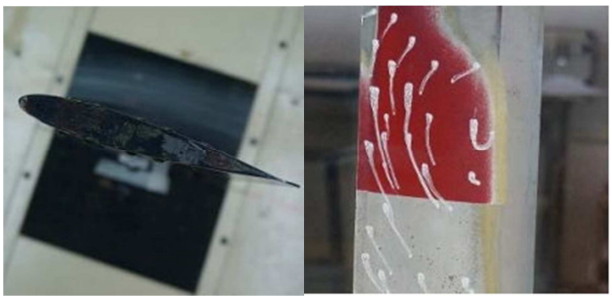

Figure 14 Smoke test and oil dot test

Although the lift force is still can be produced after that angle, the blade has a hard time to generate it. Stalling can alleviate by increasing the speed of air flow on the blade. But this will be lead to an increment of drag coefficient of tail rotor blades as show in Figure 15. After the angle of attack 12-13 degree, the drag coefficient rapidly increased, corresponds to an increment of angle of attack and speed of airflow. The coefficient of drag becomes steady after airflow speed achieved 15 m/s and above.

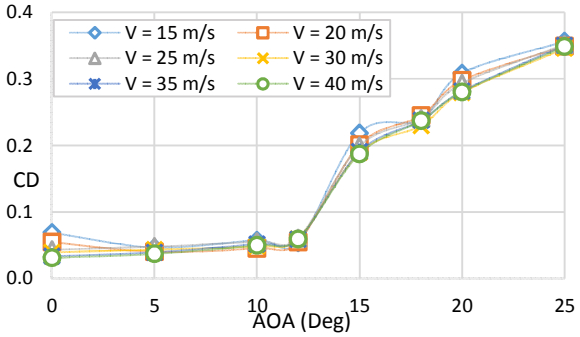

Figure 15 Drag coefficient versus angle of attack

5.2 Comparison Between CFD and Experimental Works

It is observed that the numerical results give reasonably good tendency against the ones from experimental works. This tendency starts improving with an increment of Reynolds number. The results for the drag coefficient (C_D) (Figure 16(b)) show that there is quite good agreement between the experiment and computational results. On the contrary, the prediction of computation for the lift coefficient (C_L) (Figure 16(a)) slightly overshoot against the experimental results.

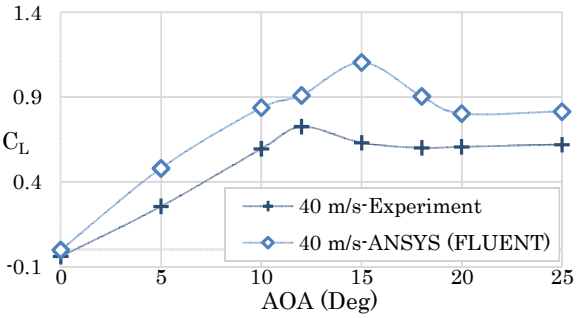

(a) Lift coefficient

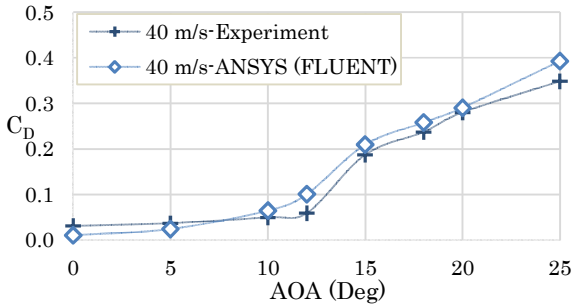

b) Drag coefficient

Figure 16 a) Comparison the lift coefficient between the experimental and simulations at airspeed = 40 m/s b) Comparison the drag coefficient between the experimental and simulations at airspeed = 40 m/s

The predictions of k–ω SST transition model do not fully agree especially for the lift coefficient (C_L) as shown in Figure 16(a) where the lift coefficient (C_L) for the simulation in higher the experimental value. This caused by the turbulence intensity that selected for simulation before is not really suitable to imitating the turbulence in wind tunnel test section. The predictions of k–ω SST transition for the lift coefficient (C_L) at low air speed was not very good but the trend and gap between simulations and experimental were improved by increasing the air speed.

In case for low Reynolds number flow conditions, predicting the drag coefficient becomes even more problematic, since low Reynolds number airfoils normally exhibit laminar separation bubbles, which are known to significantly affect the performance of an airfoil blade. As for increasing the Reynolds number, the ability of prediction of drag and lift coefficient becomes easier for the flow solvers because the flow is no longer laminar, and turbulent boundary layer is effective on the surface of the airfoil blade beginning from the leading edge.

5.3 Thrust and Torque

5.3.1 Comparison between Experimental, Simulations and Empirical Equation

It is observed (Figure 17) that the numerical simulation results give reasonably good tendency against the ones from experimental works. The results for the torque at AOA = 10^o ,12^o and 15^o, show that there is quite good agreement between the experiment and simulation results. On the contrary, the prediction of simulations for the thrust slightly overshoot against the experimental results.

By comparing the result of the experimental simulations, and empirical equation as shows in Figure 17, we found that the trend in giving the good agreement between all the data. From the tendency, we can see that, the value of thrust that calculated by empirical give the result value always lower than the experimental value. Meanwhile, the torque value becomes nearing to the value experimental due to the increasing of AOA.

Based on this result, it is clear that the empirical equation is capable of calculating predicted the thrust and torque. Maybe

only for this case, but improve can be done in feature make it reliable for any kind of propeller blade.

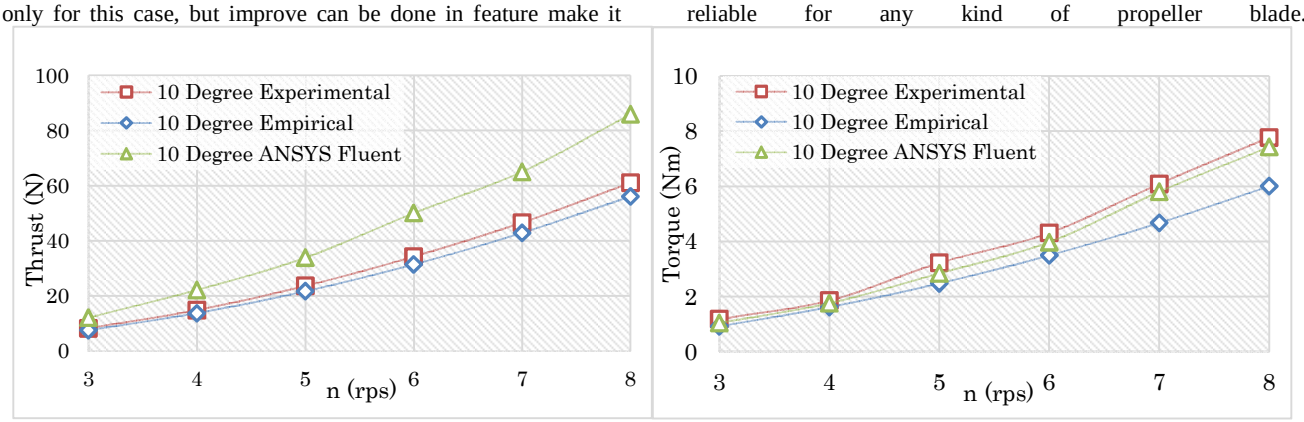

a) 10° Angle of Attack (AOA)

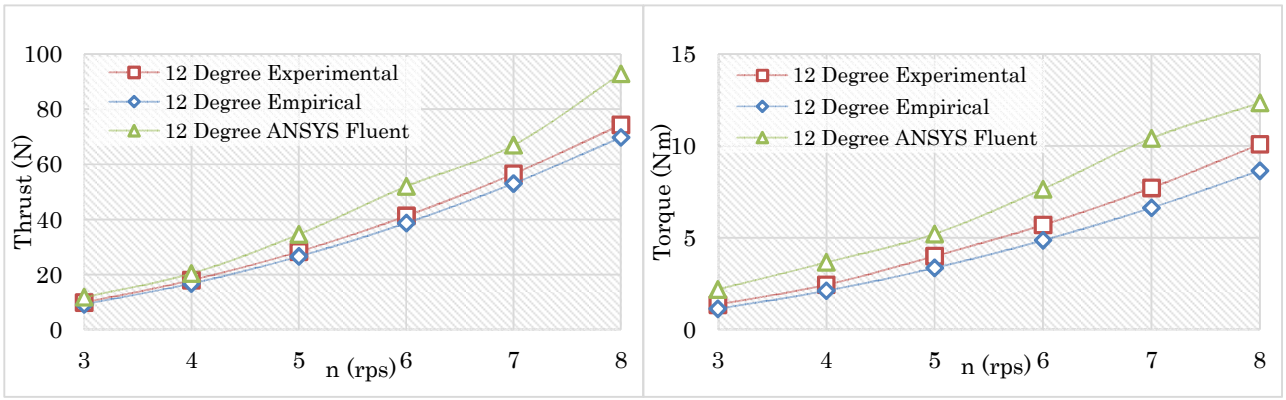

b) 12° Angle of Attack (AOA)

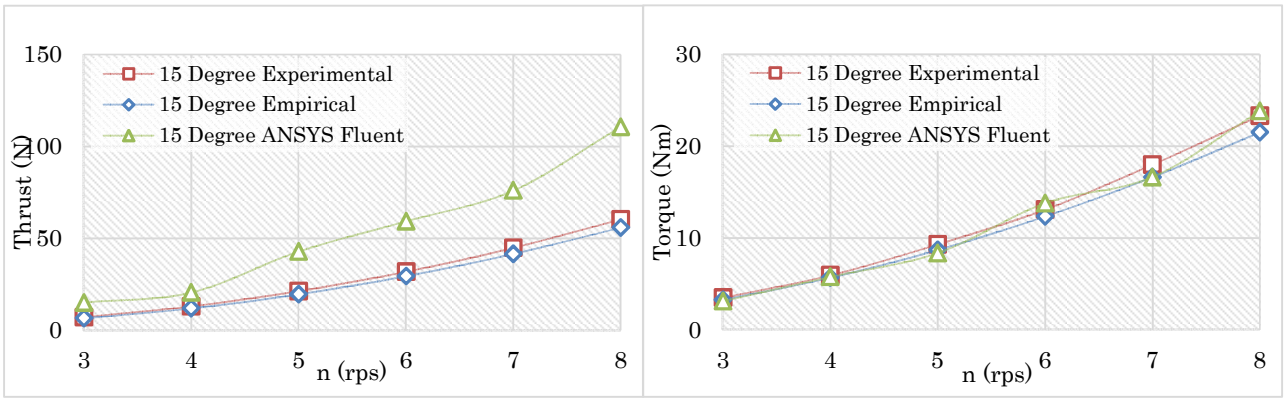

c) 15° Angle of Attack (AOA)

Figure 17 Comparisons of thrust and torque between experimental, simulation and empirical equation for a) 10° Angle of Attack (AOA), b) 12° Angle of Attack (AOA)and c)15° Angle of Attack (AOA).

6.0 CONCLUSION

During this study several assumption has been made to help this research running well without faced many complicated problem:

i. The calibration of experimental apparatus all in the best condition.
ii. Flow inside the test area is constant throughout the experiment.

iii. Grid sensitivity of mesh generation for the model considered ideal for the simulation without doing the mesh independence study.

The solutions obtained from ANSYS Fluent simulation are compared with the experimental result (Firdaus, 2015), and it is found that the prediction gives a good agreement for the trend of the lift coefficient and drag coefficient although over predict at low Reynolds number flow conditions. Furthermore, the comparison of thrust and torque were extracted from the lift and the drag value (simulation and experimental) using blade element theory (BET) and empirical numerical equation also shown they were in good agreements. Nevertheless, it is conceded that there could be discrepancies with the exact data of the 206B tail blade rotor since several assumptions had been made, and also due to some limitations of experimental and simulation works. Apart from that, in study of NACA 0012 profiles of the 206B tail blade rotor, experimental and simulation result shown it is coherent to what has been reported in some of referred thesis and journals (Jesse Wells, 2009; Douvi C. Eleni, 2012 and Katsutoshi KONDO, 2014).

ACKNOWLEDGEMENT

The authors would like express gratitude to the Department of Aeronautical, Automotive and Ocean Engineering, Universiti Teknologi Malaysia for supporting during this research implementation.

REFERNENCES

[1] John Watkinson (2003). *Art of the Helicopter*. (1st Edition). Butterworth-Heinemann.

[2] Guo-Hua Xu, Shi-Cun Wang (2001). Effects of the Shroud on Aerodynamic Performance in Helicopter Shrouded Tail Rotor System. *Aircraft Engineering and Aerospace Technology*. Vol. 73, Issue 6, pp. 568 – 573.

[3] Gordon Leishman, J (2002). *Principles of Helicopter Aerodynamics* (2nd Edition) Cambridge University Press, pp. 28-40.

[4] Young, C. (1976). *The Prediction of Helicopter Rotor Hover Performance using a Prescribed Wake Analysis.* Aerodynamics Dept., R.A.E., Farnborough, London.

[5] Antonio Filippone, (2006). *Flight Performance of Fixed and Rotary Wing Aircraft.* (1st Edition). American Institute of Aeronautics & Astronautics: Butterworth-Heinemann, pp.303.

[6] Firdaus, Jaswar Koto, I.S Ishak, M.S Ammoo (2015). Wind Tunnel Test on Generic Agusta-Bell 206B Helicopter Tail Rotor Blades. *Journal of Aeronautical -Science and Engineering-*, Vol 1, pp. 1-6.

[7] Houghton, EL., Carpenter, P.W., Steven Collicott and Dan Valentine Valentine (2013). *Aerodynamics for Engineering Students*. (6th Edition). United States: Butterworth-Heinemann, pp. 54-55, 664-669.

[8] Bramwell A. R. S., David Balmford, and George Done (2001). *Bramwell's Helicopter Dynamics*. Bath Press, Avon: Butterworth-Heinemann, pp. 46-52.

[9] Elfstrom GM. (2007). History of Test Facility Design Expertise at Aiolos, Engineering Corporation. *AIAA 45th AIAA Aerospace Sciences Meeting and Exhibit*, Reno, Nevada, USA.

[10] Alias Mohd Noor and Shuhaimi Mansor (2013). *Measuring Aerodynamic Characteristics Using High Performance Low Speed Wind Tunnel at Universiti Teknologi Malaysia.* Transport Research Alliance, Universiti Teknologi Malaysia.

[11] Mahdi Hozhabri Namin (2014). *Wind Tunnel Test to Investigate Transition to Turbulence on Wind Turbine Airfoil*. Master thesis, Universiti Teknologi Malaysia, Skudai.

[12] ANSYS Fluent (2013). *ANSYS Fluent Tutorial Guide.* ANSYS, Inc.